Check for updates

Miniature mechanical testing of LMD-fabricated compositionally & microstructurally graded γ titanium aluminides

Florian Galgon[1,a)] , **Daniel Melzer**[2] , **Christopher Zenk**[1] , **Jan Džugan**[2] , **Carolin Körner**[1]

[1] Department of Materials Science and Engineering, Institute of Materials Science and Metals Engineering, Friedrich-Alexander-Universität Erlangen-Nürnberg, Martensstraße 5, 91058 Erlangen, Germany
[2] COMTES FHT a.S., Průmyslová 995, 33441 Dobřany, Czech Republic
a) Address all correspondence to this author. e-mail: florian.galgon@fau.de

The design freedom in Laser Metal Deposition provided by the absence of a powder bed enables the fabrication of Functionally Graded Materials through Additive Manufacturing. For the first time, two suitable γ-TiAl alloys (TiAl48Cr2Nb2, TiAl45Nb4C) are combined in direct and gradual transitions to generate different microstructure morphologies and, consequently, different mechanical properties within a component after an identical heat treatment. The influence of alloy composition, microstructure type, and material transition on the tensile properties and fracture toughness is analyzed through miniature testing. Miniature tensile tests show no orientation dependency in regard to the build direction and the composition/microstructure transition is not found to be a preferred fracture site. The miniature fracture toughness tests reveal that already small composition changes—insufficient to alter the microstructure configuration—can have a significant effect on the cracking behavior.

Introduction

Lightweight intermetallic titanium aluminides were introduced into commercial airplane turbines with the maiden flight of the Boeing 787 in 2009 and will increasingly be used in turbine engines, thanks to their superior specific strength compared to Ni-based superalloys at intermediate temperatures [1–3]. The major challenges for their application and processing result from their ordered intermetallic nature which is typically associated with low ductility and toughness [3, 4]. Additionally, their properties significantly depend on the morphology and size of their major constituent phases, α_2 and γ. Fracture toughness and creep resistance are significantly higher in the so-called fully lamellar state (FL), while this configuration under most processing routes leads to a bigger grain size forfeiting the higher room-temperature ductility exhibited by so-called duplex (DUP) or nearly lamellar (NL) configurations [5]. Hence, the property profile of any TiAl microstructure configuration is necessarily a tradeoff for the application: e.g., for a turbine blade it is neither optimal for the blade fin—where maximum creep resistance would be desirable—nor the blade roots, in which maximum ductility would be desirable. This resulting compromise has to

be compensated with thicker material cross-sections, reducing the possible weight savings.

Their low ductility makes them hardly processable by conventional means. Specialized casting processes like centrifugal casting are needed to produce ingots or simple geometries of which the cross-section decreases continuously in one direction [3]. Another possibility is hot extrusion of cast ingots or atomized and canned powder. If the extrusion temperature is above the γ solvus temperature of the alloy extremely fine lamella and colony sizes develop [6], but the high temperatures around 1300 °C render it technologically demanding. Forging of TiAl alloys is very challenging and conducted almost exclusively on special alloys developed for this purpose (referred to as TNM), in which the unordered, cubic β phase is stable at high temperatures. The forging temperature has to be above 1150 °C and followed by careful heat treatments to reduce the unordered phase content and limit the formation of detrimental β_0 and ω_0 phases as much as possible [7]. The challenges associated with conventional casting and forging techniques are the reason for the high interest in additive manufacturing of TiAl alloys and allows complex geometries like turbocharger wheels
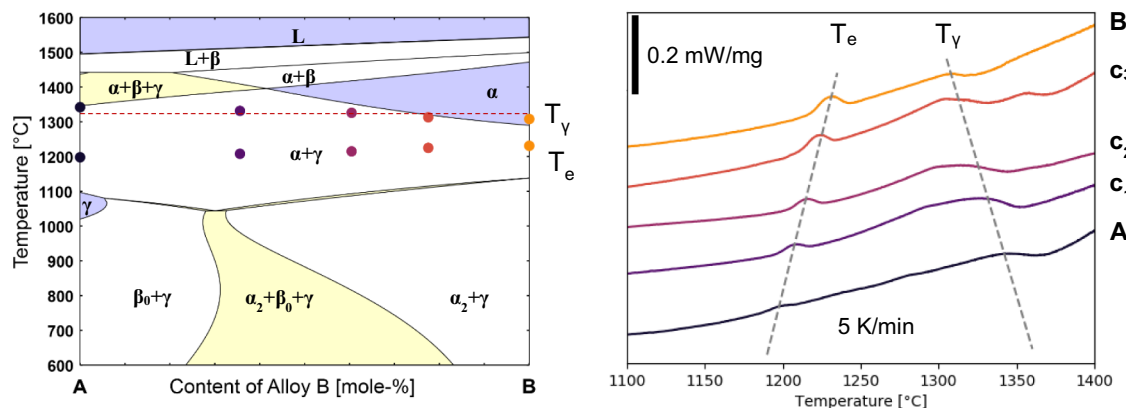
Figure 1: Pseudo-binary phase diagram (left) between the two alloys (A) TiAl48Nb2Cr2 and (B) TiAl45Nb4C calculated using Thermo-Calc and the TCTI2.2 database, and DSC heating curves (right) of the two alloys and three intermediate compositions in the as-built condition, the transformation temperatures are overlaid in the phase diagram with the same color, and the heat treatment temperature of 1320 °C is marked by the dashed line.

using powder bed fusion (PBF) processes with an electron beam [8–10] or laser source [11] and direct energy deposition (DED) processes [12, 13].

The aim of this study was to combine two alloys—TiAl-48Cr2Nb2 and TiAl45Nb4C[1]—in the additive manufacturing process Laser Metal Deposition (LMD). Alloy compositions and subsequent heat treatments are selected in order to produce different microstructure configurations—with the associated mechanical properties—in different parts of a manufactured sample. Processing two powders together this way is not possible in PBF processes without rendering all unmolten powder unusable due to intermixing and henceforth unknown composition. If successful, this would allow the fabrication of a component with locally tailored properties, to suit locally varying requirements.

In the case of additively manufactured materials miniature testing is especially suited for the evaluation of local material properties [14], particularly when functionally graded materials (FGM) are examined, which are characterized by local material interfaces or areas with different structural features. Miniature tensile testing (MTT) application of additively manufactured components was demonstrated earlier in [15]. However, the miniaturization effects need to be taken into account when the results are presented, e.g., number of grains within the specimen cross-section [16, 17].

Results and discussion

Calphad & differential scanning calorimetry

Calphad was used to identify compositions for which a temperature exist at which one alloy is in the α single-phase field,

while the other is in the $\alpha + \gamma$ phase field. After heat treating at and cooling from this temperature, the former alloy will be fully lamellar (FL), while the latter will form a duplex (DUP) or nearly lamellar (NL) microstructure. As shown in Fig. 1 left, the alloys A TiAl48Cr2Nb2 and B TiAl45Nb4C selected fulfill this criterion at 1320 °C that is chosen as our standard heat treatment temperature. Additionally, the results of the DSC measurements on the two alloys and the three intermediate compositions c_1, c_2, and c_3, as determined by EDS, are shown in Fig. 1 left. The experimentally determined phase transition temperatures T_e and T_γ are indicated in both graphs.

The existence of the afore-mentioned temperature region is experimentally proven by DSC. In contradiction to the Calphad simulations, the γ solvus temperatures (T_γ) decrease continuously from alloy A to B, while eutectoid temperatures (T_e) increase. *Thermo-Calc* wrongfully negates the existence of a α single-phase field for alloy A, which is evident in the DSC results and the microstructure after an heat treatment at 1360 °C that is shown in Fig. 2(c). Also, no presence of β phase or its variants was experimentally confirmed in both alloys which consist of $\alpha_2 + \gamma$ at room temperature. To further illustrate the unreliability of the TCTI2 database for alloy A see Figure S 1 of the supporting information, showing calculated phase content depending on temperature for this fixed composition. While it is unclear why our DSC experiments overestimate the α_2 to α disordering reaction temperature (occurs at T_e) by about 80 to 100 K compared to the literature [18], our T_γ—which are of greater importance for the design of a suitable heat treatment—are in good agreement.

Microstructure

As we want to create the greatest possible property differences through heat treatment, we first have to look at our starting

---

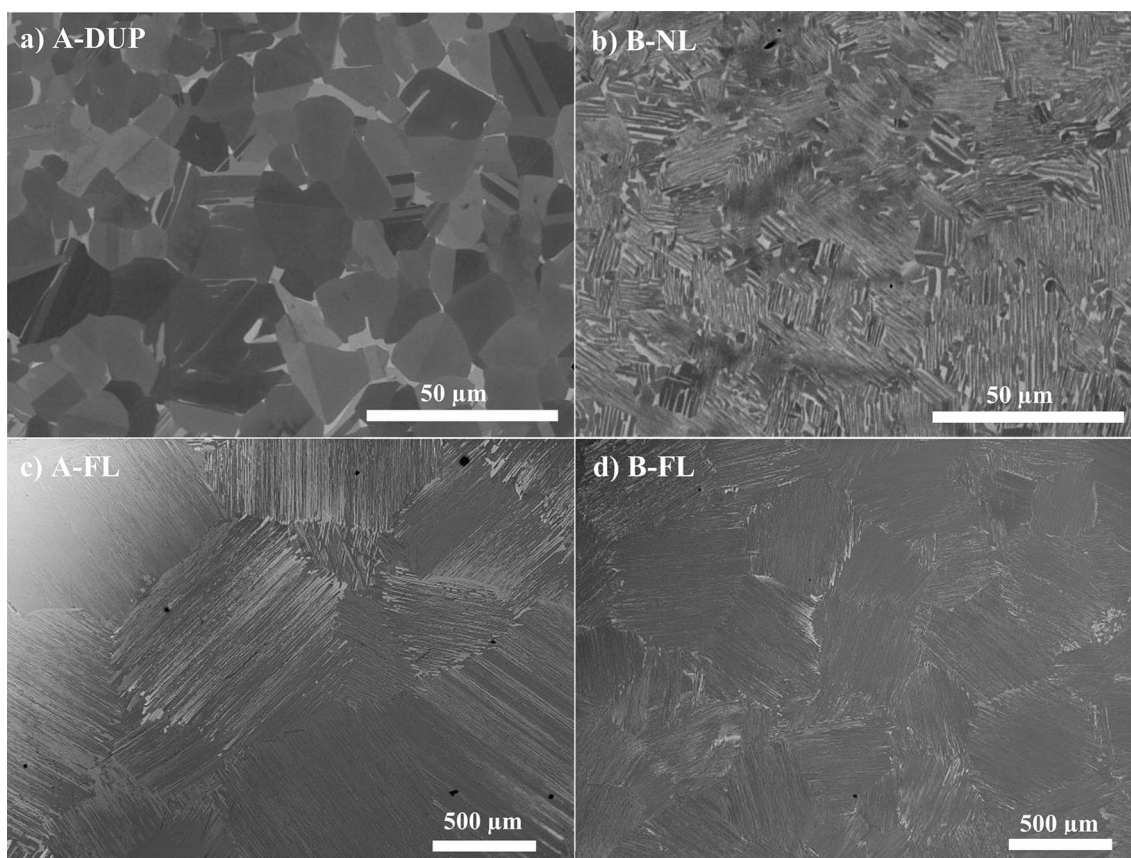[1] Compositions in at.% if not specified otherwise.

Figure 2: Microstructures of the two alloys after heat treatments at different temperatures followed by furnace cooling results in (a) A-DUP @ 1320 °C, (b) B-NL @ 1200 °C, (c) A-FL @ 1360 °C, and (d) B-FL @ 1320 °C.

TABLE 1: Grain and colony sizes of the two alloys after heat treatments at different temperatures to reach the desired microstructure types.

	Composition	Microstructure	HT temperature	Average feature size	Max feature size
A	TiAl48Cr2Nb2	DUP	1320 °C	8.4 ± 1 µm	20 µm
		FL	1360 °C	576 ± 188 µm	1360 µm
B	TiAl45Nb4C	FL	1320 °C	298 ± 46 µm	400 µm
		NL	1200 °C		25 µm

point in the as-built condition, as it determines what microstructures are achievable through heat treatment.

As-built condition

In the non-equilibrium state after LMD processing, alloy A exhibits a higher amount of globular gamma and less as well as smaller lamellar colonies compared to alloy B, and the morphologies are categorized as duplex for alloy A and nearly lamellar for alloy B. Micrographs are shown in Figure S 3 of the supplementary material. Assuming that the identical LMD parameters used for both alloys lead to the same temperatures during processing, this can be explained with the DSC results, as they show that at any given temperature, the γ phase fraction is lower in alloy B. Therefore, the α grains can grow to larger sizes in the

in situ heat treatment during the deposition of subsequent layers and the nearly lamellar morphology is established.

Heat-treated condition

Additional to the heat treatment at 1320 °C, monolithic blocks should also be heat treated to inverse microstructures. For alloy A-FL morphology was archived by a heat treatment at 1360 °C. From the as-built microstructure of alloy B discussed before, it is not possible to reach a duplex morphology, so a heat treatment at 1200 °C was chosen to reach annealed NL morphology.

Table 1 lists the feature size, meaning colony or γ grain size, measured after heat treatment by the line intersection analysis. Figure 2 shows representative micrographs. In B-NL colony and γ grain boundaries are barely discernible, which is
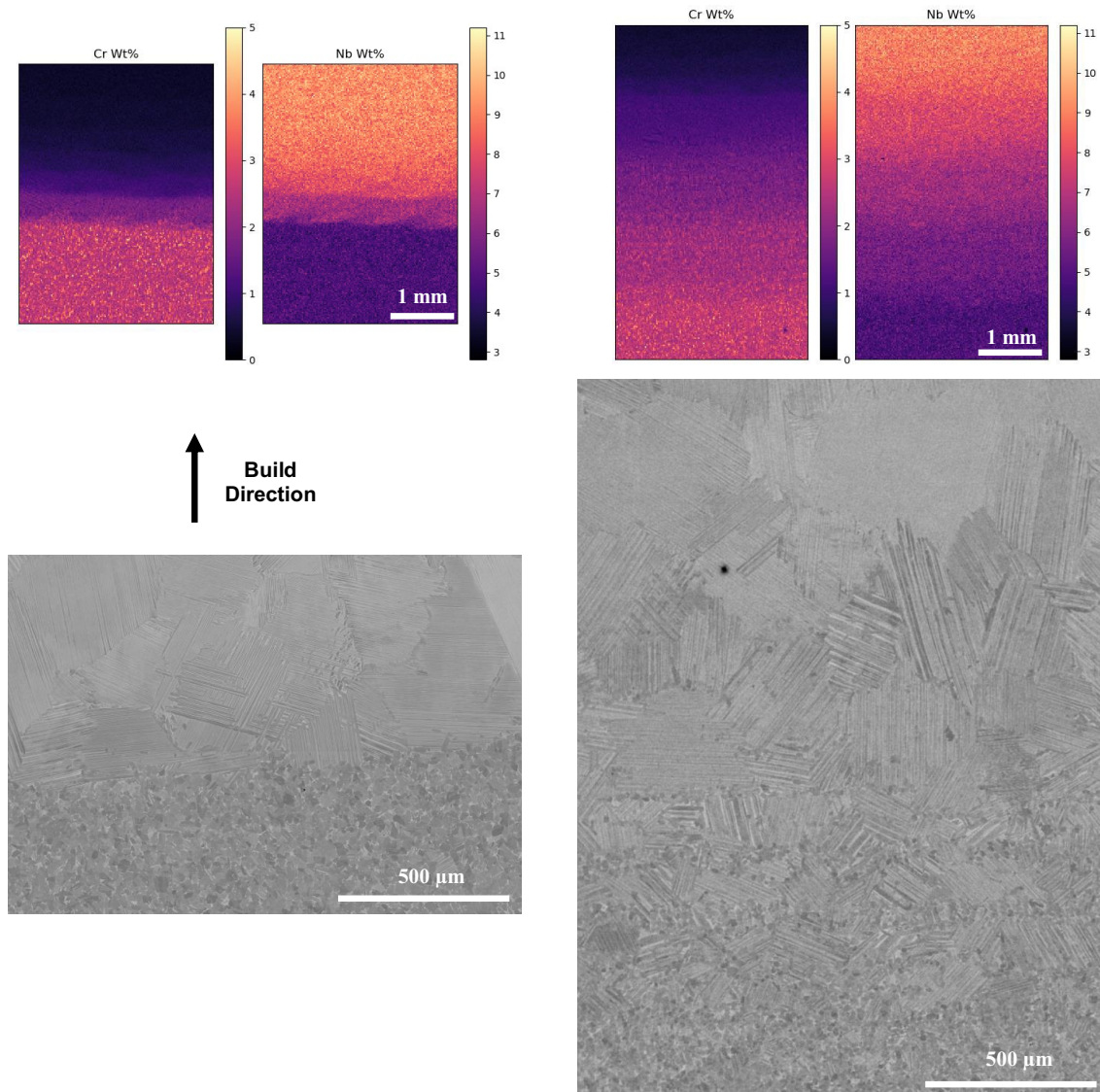
Figure 3: EPMA mappings of the alloying elements chromium and niobium (top) and corresponding microstructures (bottom). Direct transition AB (right) and graded transition A|||B (left) after heat treatment at 1320 °C.

why only a maximum feature size was estimated. A-DUP and B-NL never reached a single-phase field during heat treatment and therefore feature size remains small and on the same order of magnitude. That is why it is feasible to compare A-DUP and B-NL to each other and contrast them with A-FL and B-FL, as differences in the mechanical properties of duplex and nearly lamellar morphologies with the same feature size are minimal in contrast to coarser fully lamellar morphology [5]. To reach a FL microstructure in alloy A, a higher heat treatment temperature was needed, which led to faster α grain growth in A-FL compared to B-FL resulting in a nearly twice as high colony diameter after cooling.

Composition and microstructure gradients

The composition changes between the two alloys measured by EPMA are shown in Fig. 3 for the AB direct and the A|||B-graded transition. Even though the powder supply was switched from 100% A to 100% B in the AB specimens, intermixing is obvious for two layers, followed by a third one where it is still discernible to a lesser degree. For a full metallurgical bond in laser welding between the substrate and the deposited material, the substrate has to be partly molten. It is well known that a dissimilar substrate leads to dilution of the first deposited layer. Through the layer-wise manufacturing in LMD, the last layer deposited becomes
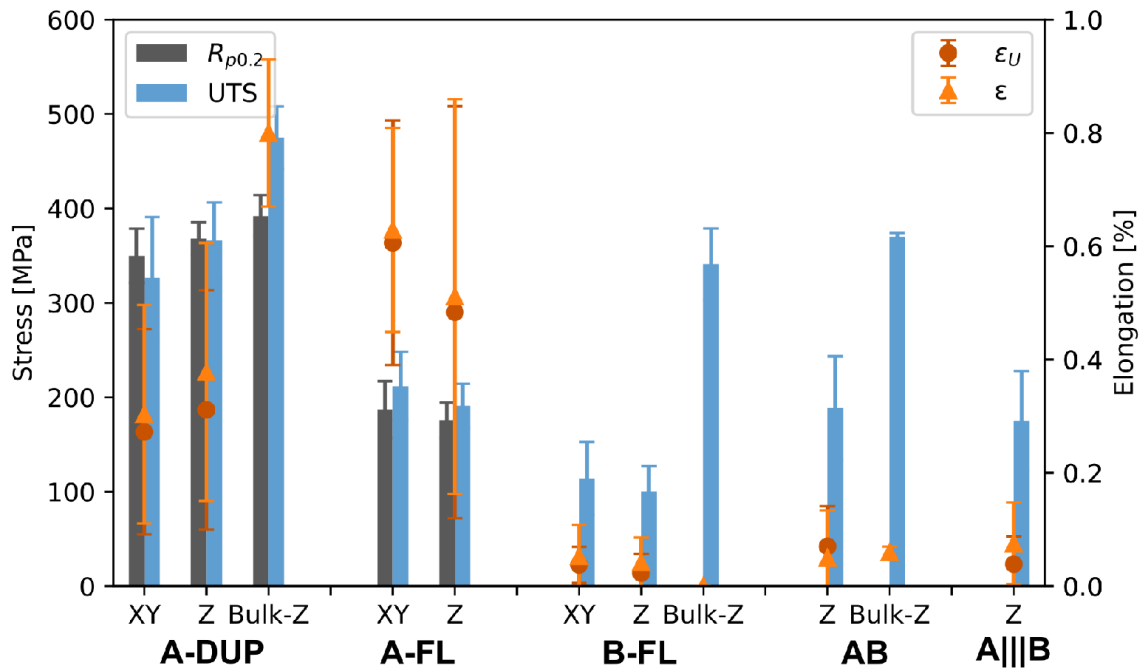
Figure 4: Overview of offset yield strength $R_{p0.2}$, tensile strength UTS, uniform elongation ε_U, and total elongation ε results for all batches. Monolithic miniature tests were done in XY- and Z-direction. AB and A|||B were specimens with an alloy and microstructure transition in Z-direction.

the substrate for the next layer and the dilution gets weaker with each layer. During multi-material LMD, the same phenomenon happens each time the individual powder feed rates are adjusted, which is why the transition in A|||B does not occur in 3 sharp steps, but while the steps are distinguishable, the composition changes rather gradually.

Even though in the chemical composition the LMD layers are visible as multiple steps, the microstructure configuration changes suddenly for the direct transition AB specimen that is also shown in Fig. 3. This is because the γ solvus temperature continuously drops with the change of composition from A to B. Once a single-phase region is established during heat treatment, the α grains grow and transform to lamella on cooling. In the graded transition samples A|||B the microstructure follows the gradual chemical composition change somewhat, with an intermediate area that can be designated as nearly lamellar. However, the extent of the 0.6–0.8-mm-wide microstructural transition zone is notably smaller than the 2.6-mm-wide chemical transition.

Tensile properties

The results of the tensile tests will be presented in three stages: (i) tensile properties for MTT specimens A and B with uniform composition but different microstructures, including anisotropy in regard to the built direction, (ii) comparison of miniature and bulk tensile results, and (iii)

composition and microstructure gradients AB and A|||B. The total number of specimens tested per condition is listed in Table S1 of the Supporting Information, where also Table S2 can be found with the characteristic values plotted in Fig. 4.

Monolithic miniature tests

A-DUP reaches the highest tensile strength values followed by the same alloy in FL configuration trailed by B-FL, as can be seen in Fig. 4. The differences between the two A configurations are in accordance with the detrimental effect of the colony size of the FL microstructure on the room-temperature strength [5]. That B-FL shows even lower values even though the colony size is smaller can be explained by the alloy composition design that was optimized for creep properties. For example, it excludes chromium, which improves the room-temperature mechanical properties as discussed in the same paper, while 0.5 at.% Carbon is added obstructing dislocation movement.

As far as elongation is concerned, the B-FL specimens fail at a maximum of 0.1% strain, while A-FL specimens failed between 0.1 and 1% with mean values of 0.6% in XY- and 0.5% in Z-orientation. Compared with A-DUP, where no difference between XY and Z can be detected, the mean values (0.2%) were lower, while the standard deviation remains the same. That A-FL specimens reach higher elongation values than A-DUP contradicts the findings of Kim et al. [5] and cannot be explained by miniaturization effects, as A-DUP has the lower feature size with more grains in the cross-section. However, since our values are very

low and the standard deviation is very high, no further conclusions can be drawn at this stage.

These low failure elongations mean that the offset yield strength $R_{p0.2}$ could only be determined for specimens reaching higher elongation which coincided with higher tensile strength. That is why the yield strength means are higher than the tensile strength means for A-DUP. For specimens where yield strength could be determined tensile strength was at average 17 ± 6 MPa higher than yield strength. The higher elongation reached by A-FL allowed for yield strength determination for all but two samples.

Despite alloy composition and microstructure differences in no case an orientation dependency in regard to the build direction could be observed. The scattering bands of all characteristic values in XY- and Z-orientation do overlap and there is no trend in the average values.

Bulk comparison

A considerable decrease of the tensile strength values for miniature versus bulk tests can be seen for all sets in Fig. 4. A-DUP is the only variant where yield strength can be compared between miniature and bulk testing, and the mean values of the miniature tests are lower but the scattering band still overlaps with the bulk values. Tensile strength determined from miniature test specimens on the other hand are significantly lower. One factor which might be responsible for that is the early fracture phenomenon. A combination of the material brittleness and the employed MTT geometry—which due to the small amount of available material required a relatively small specimen neck curvature radius—seems to have a considerable effect on the fracture process of brittle materials. Analysis of the fracture locations revealed that most of the specimens failed in close proximity of the shoulder. It suggests that the radii act as spots of stress concentration during the test which should lead to premature failure at values smaller than the ultimate tensile strength. This is consistent with the fact that no reduction of the cross-section area was measured after the test, and the yield strength is only marginally affected by the miniaturization for the materials investigated.

The values we find for yield strength and elongation of A-DUP are by 25 MPa and 0.4% to 0.9% lower than those reported for LMD-processed TiAl47Cr2Nb2 (421 MPa & 1.7% in XY and 431 MPa & 1.2% in Z) [19]. In their bulk tensile tests, they could detect a difference in elongation and tensile strength for XY- and Z-orientation. To draw a further comparison with PBF-EB-produced TiAl alloys, Lin et al. [20] investigated PBF-EB-produced TiAl48Cr2Nb2 after hot isostatic pressing and additional heat treatment to reach duplex microstructure lead to a yield strength of 360 MPa and 2% elongation in XY and 380 MPa and 1.2% elongation in Z-direction, while both reached 480 MPa tensile strength. Also for other microstructure

configurations they tested that XY-orientation always showed lower yield strength but higher elongation and tensile strength. So our LMD-produced A-DUP results show the same tensile strength combined with higher yield strength but lower elongation and for PBF-EM-produced B-FL our previous work found equal tensile strength and minimal fracture elongation of 0.15% [21].

Gradient specimens

Specimens AB and A|||B after multi-material processing were tested to determine if the alloy composition and microstructure transition have a detrimental effect on the properties. The results are also included in Fig. 4. Generally, the tensile strength and elongation values of the graded materials lie in between of the ones for A-DUP and B-FL. The fracture elongation was 0.05% for AB and 0.08% for A|||B and no yield strength could be determined.

The fracture location of MTT specimens was analyzed by EDS. For the gradual transition A|||B one failure occurred at an intermediate composition, while the other three broke on the B-FL side. The interpretation for the direct transition batch AB is more complicated, because (i) the transition in most samples is very close to one end of the gage length and therefore the gage nearly consist of only one alloy and (ii) fracture occurred in the radii close to the shoulders for six out of the eight MTT specimens. Out of those six specimens, two failed close to the material transition on the B-FL side. This makes it unclear if the material transition or the stress concentration of the radii leading to an early fracture phenomenon had the decisive influence. Three failure locations each could be identified clearly in either A-DUP or B-FL.

The bulk direct transition specimens AB reached identical tensile strength values of the bulk B-FL ones, while elongation was minimally higher, with fracture occurring only on the B-FL side. This confirms the trend seen in the MTT results before that the material and microstructure transition are no weak point, which is a promising finding for the development and production of compositionally and functionally graded TiAl components.

Fracture toughness

The fracture toughness results for all material types are summarized within this section. Representative force-load line records are depicted in Fig. 5. The corresponding average K_{IC}, K_Q, and K_{JC} values with standard deviations are listed in Table 2. The number of valid K_{IC}/K_Q results per condition is presented with a note how many of them met the conditions of validity. Validity condition I is met when $F_{max}/F_Q < 1.1$, where F_{max} is the maximum loading force and F_Q is the force evaluated using secant line method. As can be seen from the table, the condition was
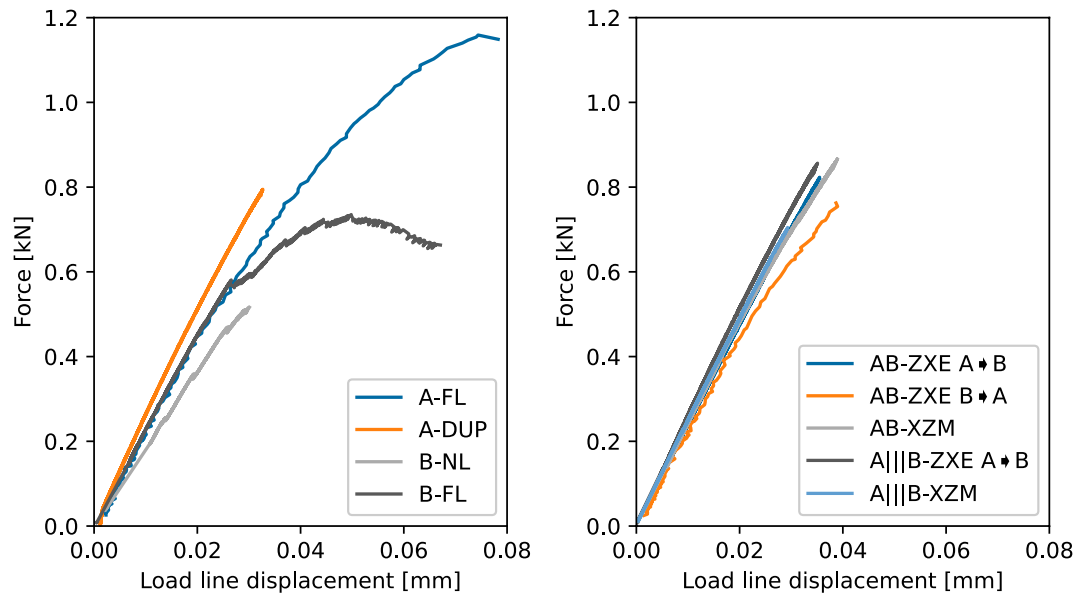
Figure 5: Representative force-load line records for all tested material batches. Monolithic alloys A and B were tested in two microstructure configurations, direct transition AB and graded transition A|||B specimens perpendicular (ZXE) and parallel (XZM) to material and microstructure transition.

TABLE 2: Summarization of the fracture toughness results based on the three different evaluation methods and calculated plastic zone size.

	Microstructure	Orientation	K_{IC}/K_Q (F_Q) MPa m$^{1/2}$	Validity condition I	Validity condition II	K_{IC} (F_{max}) MPa m$^{1/2}$	K_{JC} MPa m$^{1/2}$	Plastic zone size μm
A	DUP	ZXE	12,1 ± 1.3	0/3	3/3	15.2 ± 0.6	18.2 ± 1.6	111
	FL	ZXE	12.4 ± 1.5	0/5	5/5	18.3 ± 3.0	29.9 ± 7.2	117
B	FL	ZXE	10.0 ± 1.4	0/4	4/4	14.5 ± 1.6	23.9 ± 4.7	74
	NL	ZXE	8.0 ± 2.0	1/3	3/3	9.5 ± 0.4	11.5 ± 0.7	48
AB	DUP/FL	XZM	13.8 ± 1.1	1/4	3/4	16.2 ± 0.9	17.5 ± 1.2	144
		ZXE B → A	11.8 ± 0.4	1/4	4/4	14.2 ± 1.7	17.9 ± 4.0	116
		ZXE A → B	12.9 ± 1.7	2/4	3/4	15.9 ± 0.2	17.0 ± 1.6	157
A|||B	DUP/FL	XZM	–	4/4	4/4	12.2 ± 1.1	12.8 ± 1.0	111
		ZXE A → B	13.8 ± 0.8	2/4	3/4	16.0 ± 1.0	17.4 ± 1.0	144

not satisfied in all tests, and in the case of XZM-oriented A|||B specimens were not applicable since there was no intersection between secant line and test record. Validity condition II refers to the expression $2.5(K_{IC}/\sigma_y)^2$, which must be greater than specimen thickness or ligament. This condition verifies whether the plane strain condition was satisfied. Validity condition II was satisfied for alloy A specimens, which exhibit satisfactory yield strength values. In the case of alloy B and graded materials AB and A|||B, it was not possible to determine the yield strength for reasons that are addressed in Sect. "Monolithic miniature tests." Therefore, it was replaced with tensile strength in the expression. Nevertheless, the values were insufficient for some specimens to satisfy the second condition. As described in the methods section, fracture toughness was also evaluated using the J-integral. It can be seen, that the most conservative secant line method results

in the smallest K_{IC} values. The other two evaluation methods using the maximum force and the J-integral approaches resulted in overall higher values.

It should be emphasized that due to the extreme brittleness of the materials, the MCT specimens were tested without pre-cracking and side grooves, even though this is not the conventional approach for fracture toughness determination.

Monolithic specimens

The difference between test records of A-DUP and B-NL compared to the same alloys in FL configuration is remarkable. While the globular structured specimens showed a noticeable linear trend in the force-load line plot, the FL specimens were characterized by a certain tendency to distinct stable crack growth that is also reflected in considerable higher K_{JC} values.
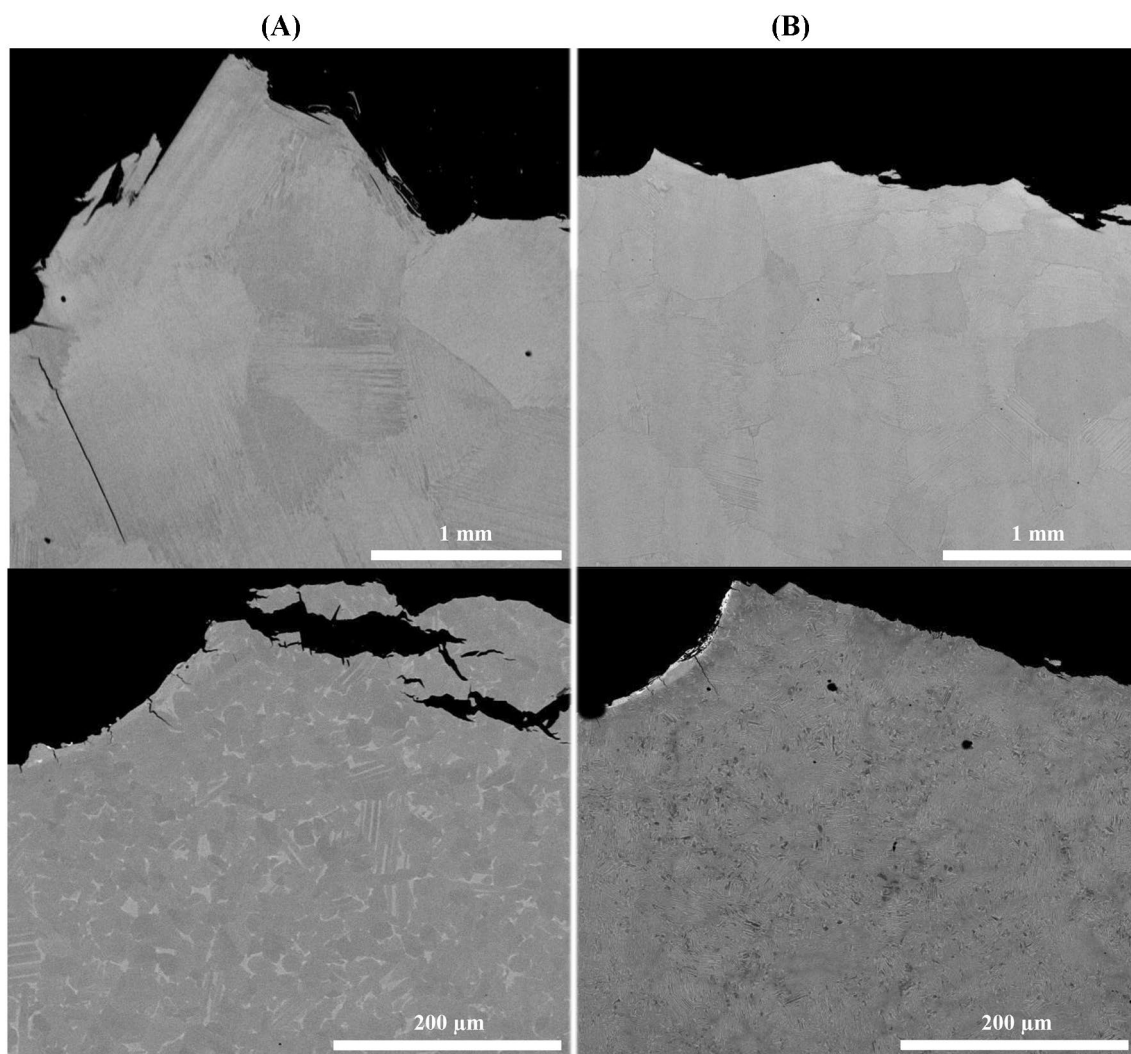
(A) (B)

Figure 6: Cross-sections through monolithic specimens of A (left) and B (right) in fully lamellar (top) and duplex/nearly lamellar (bottom) morphology.

In the cross-sectional micrographs of both A-FL and B-FL specimens shown in Fig. 6, the cracks run mostly either around colonies or parallel to the lamellas, with additional delamination of neighboring lamellas. A colony oriented roughly perpendicular to a crack either deflects the crack—prolonging its path—or completely stops this crack path while a new crack forms, leading to micro-crack formation toughening as well as shear ligament shielding [22, 23]. This finding demonstrates that interlamellar and intergranular toughness are significantly lower than translamellar. At the colony borders, often a broad γ lamella is found, e.g., Figure S 10 of the Supplementary Information. This could explain the tendency for intergranular cracking, as the γ phase has a low intrinsic K_{IC} of 10 MPa m$^{1/2}$ [24].

In the more globular A-DUP and B-NL microstructure types the cracks still run predominantly along colony or grain borders as can also be seen in Fig. 6, but since the relevant feature size is one to two orders of magnitude smaller the crack path deviations are minor.

The plastic zone size at the notch tip is calculated as $r_{pl} = (1/6\pi) \times (K_{IC}/\sigma_y)^2$ and the diameter of the zone in μm is presented in Table 2. It is evident that the plastic zone is on the one hand considerably smaller than the FL colonies sizes, but on the other substantially bigger than the duplex or nearly lamellar feature size. In fully lamellar material it seems that the crack initiation and propagation are more dependent on the unfavorable orientation of the colony with respect to the crack propagation direction. In case of the more globular structures, the crack initiation is easier since the grains are significantly smaller than the plastic zone. It seems that in both cases transgranular cracking is dominant.

Lou and Soboyejo [22] suggest that toughening was due to ligament bridging and with weighted small- and large-scale bridging they could model this toughening contribution very
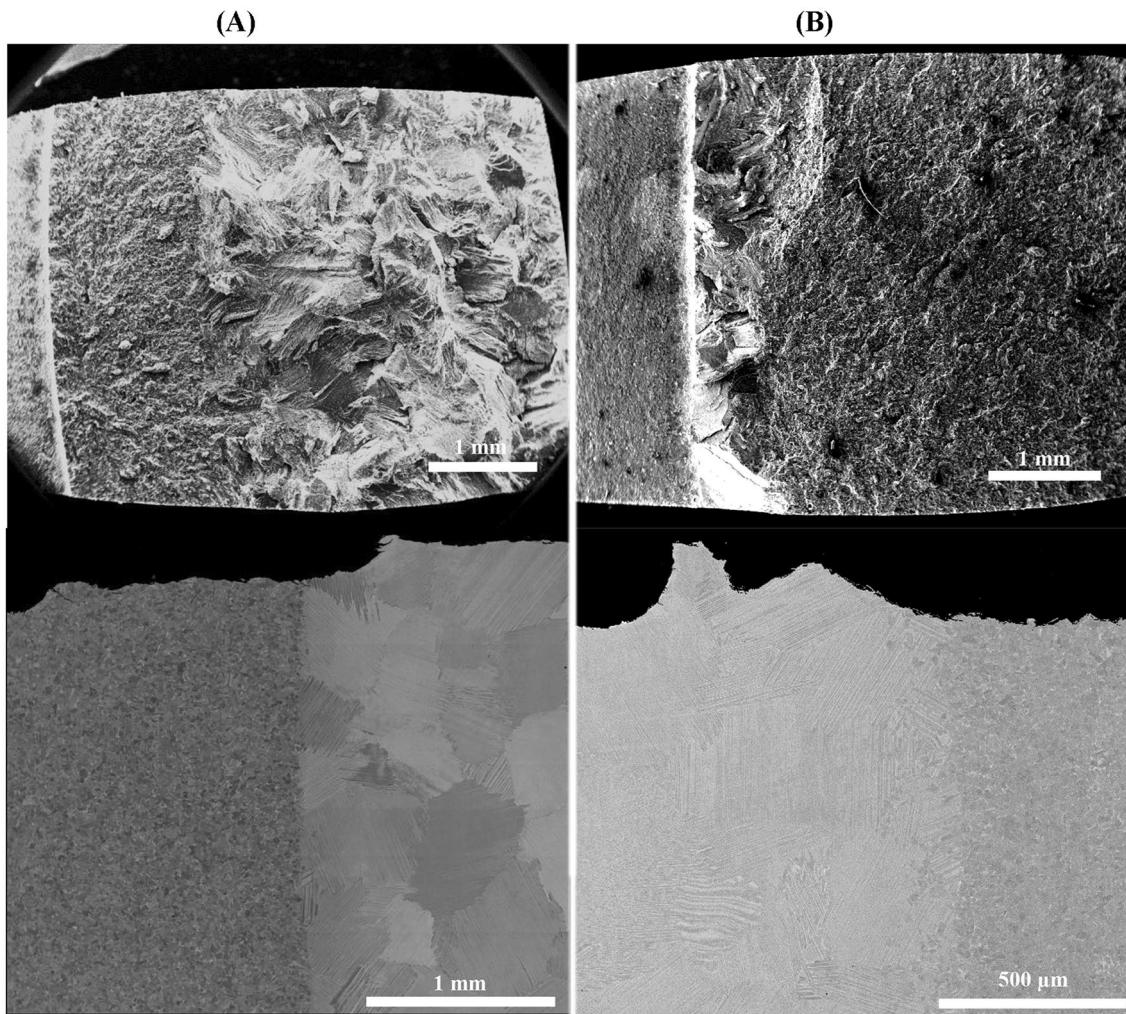
(A) **(B)**

Figure 7: Fracture surfaces (top) and cross-sections (bottom) of direct transition specimens AB in ZXE orientation, meaning perpendicular to transition, notch from A → B (left) and from B → A (right).

well. This contribution is dependent of the yield strength of the material. This is in line with the fact that our B specimens failed in tensile testing before the yield strength could be determined and therefore show lower SIF values than A specimens in a comparable microstructure configuration.

Evaluated SIF values within the current study are in very good agreement with the results presented by other studies, for the fully lamellar structures [22, 24] and globular structures [23, 25]. The major microstructure configuration influence put up by [5] is clearly shown, with roughly about double the K_{JC} values for the fully lamellar morphologies. Furthermore, within the study by Lintner et al. [25], the specimens' notches were prepared by razor blade polishing and short fatigue pre-cracking. Despite this fact, the K_{IC} is in good agreement, which points out that the presence of the pre-crack only has a minor effect on the fracture toughness. However, this seems to be applicable only to the fracture toughness measured at

the quasi-static loading mode since the study of Eck et al. [26] demonstrated the importance of the notch preparation in the case of fatigue crack growth process. This is caused mainly by the different level of micro-cracks that formed. Furthermore, the actual SIF value turned out to be overestimated, when cracks smaller than half of the notch radius are present. However, the effect of micro-cracks might be less distinct in the case of the quasi-static loading process. Another study by Akourri et al. [27] was focused on how the notch geometry affects the J_{IC} value. In this article and in previous works cited in therein, it was demonstrated that J_{IC} increases linearly with the root radius.

Gradient specimens

The fracture toughness was also investigated for graded materials AB and A|||B—to the authors' knowledge—for the first time. The aim was to perform tests with the crack growing within
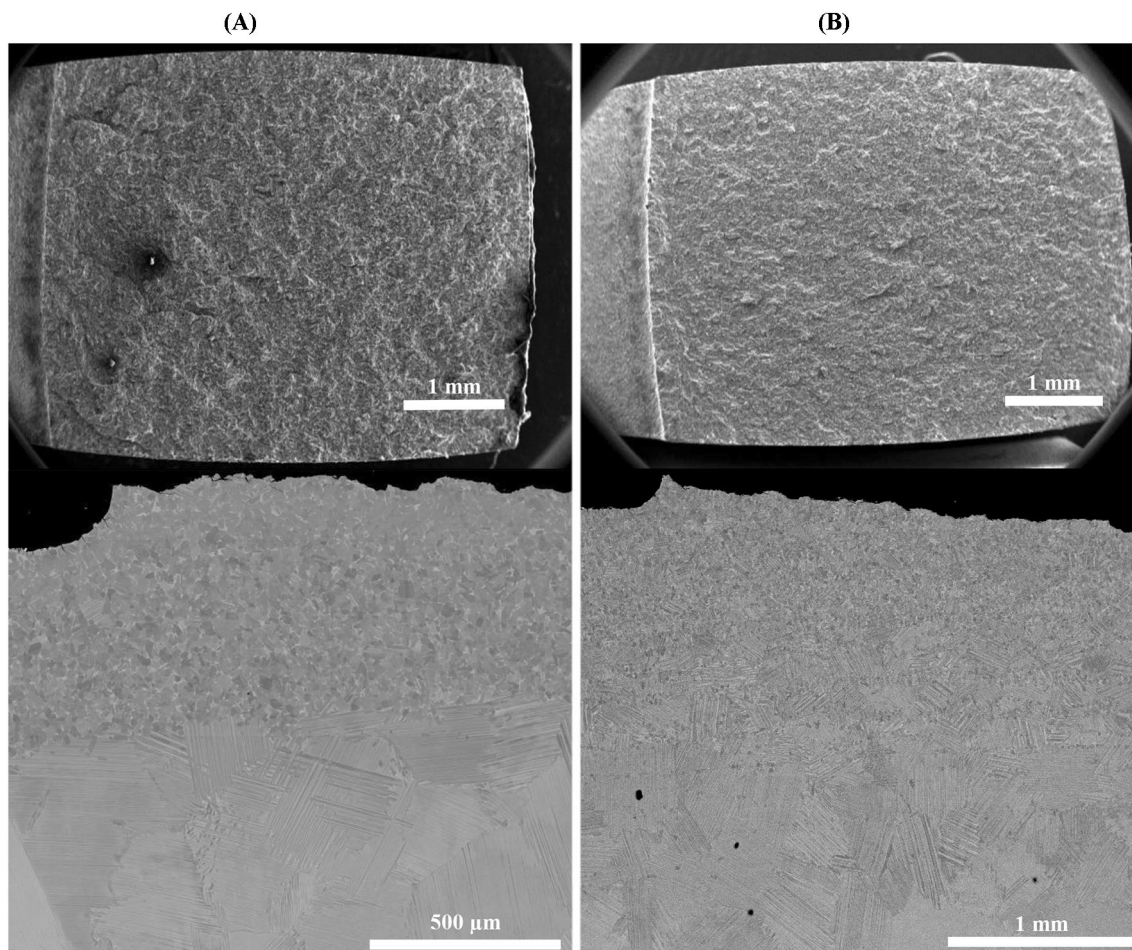
(A) **(B)**

Figure 8: Fracture surfaces (top) and cross-sections (bottom) of specimens in XZM orientation, meaning parallel to transition for direct transition AB (left) and gradual transition A|||B (right).

the material interface (XZM) and across the material interface (ZXE). For the ZXE orientation with the crack originating in the A-DUP part, a rather straight crack path is observed for the duplex zone in the cross-section in Fig. 7. After the transition to the fully lamellar structure this crack direction is not changed at first and the first colony is cracked translamellar. Then the crack gets deflected around a diagonally oriented colony in intergranular fracture mode, after which the next colony then fractures translamellar again. It has to be kept in mind that this is only one 2D section of the 3D specimen and the cracking of the fully lamellar part was already part of the fatal failure. The SIF values for ZXE A→B did not capture any shielding effect or tendency to stop the crack propagation by the fully lamellar part during data recording before the fatal crack. No effect of the fully lamellar portion of the specimens could be measured, all values including standard deviation are on the level of monolithic A-DUP.

If the crack originated from the fully lamellar side ZXE B→A, the crack was deviated by the lamellas and the crack path prolonged as seen in Fig. 7. While the mean values of K_{IC}

and K_{JC} are nearly identical to the opposite crack direction, the standard deviations are as high as otherwise only in monolithic FL specimens, so there seems to be an influence of these few colonies, but as they are so few, their individual orientation leads to a wider distribution. For ZXE orientation no differences in the values of AB and A|||B could be found, even though A|||B was the only batch in which there was no intersection between secant line and test record.

Figure 8 shows fracture surfaces and cross-sections of XZM-oriented specimens. The morphology transition for the direct transition specimens AB was missed by around 500 μm, leading to the notch lying fully in the A-DUP region. Therefore the K_{IC} and K_{JC} values are identical to those of A-DUP. For the graded transition A|||B XZM specimens EDS measurements like Figure S 12 in the Supporting Information showed that the notch was in the first A-rich gradient segment, where the composition change is not yet big enough to lead to a microstructure change, so it is still in duplex configuration. K_{IC} and K_{JC} are lower than for AB XZM or A-DUP, which can be explained with the composition

influence, as B-NL has about a third lower SIF values as A-DUP as discussed before. Therefore the results of the gradient A|||B and monolithic A and B specimens reinforce each other.

Conclusion

Two γ titanium aluminide alloy compositions were identified that allow the realization of a dual microstructure of duplex and fully lamellar configurations in one component after heat treatment at a common temperature. Both alloys and transitions between the two could successfully be produced dense and crack-free through LMD without additional heating for the first time.

Miniature tensile testing showed no orientation dependency in regard to the build direction and the composition & microstructure transition were not revealed as a weak point in tensile testing. Miniature and bulk tensile testing showed the same trends between the different specimen batches, even though the tight radii in the miniature specimens lead to early fracture and therefore lower tensile strength values. Where yield strength could be determined it was in good agreement between miniature and bulk testing.

Regarding miniature fracture toughness testing the results for compositionally uniform specimens are in good agreement with conventional bulk specimens. On top of the microstructure influence, significant differences between the two alloys in comparable microstructures could be measured and explained. Furthermore the transition between two γ-TiAls could be tested for the first time, despite the fact that positioning of the notch at the material interface is very challenging. Even more so combined with the brittleness and low toughness of γ titanium aluminides that lead to low crack extension during testing. It was shown that in the gradual transition not only the microstructure transition, but also the previous composition steps have an influence, which is in accordance to the results of the compositionally uniform specimens. For the combination of the two alloys and the heat treatment chosen in this study, this means that toughness is the lowest in the transition zone. The cause is that in the same microstructure alloy A has the higher toughness, but after the chosen heat treatment for the graded specimens it shows the less tough duplex microstructure configuration. Diluting it with alloy B to an extent that does not change the microstructure configuration, lessens toughness. The gradient segment has to reach a composition that lies in the single-phase field during the heat treatment therefore changing the microstructure to than increase the toughness greatly.

Materials and methods

LMD fabrication

The additively manufactured samples were produced via a directed energy deposition (DED) process as categorized by

ASTM F2792-12a [28] using an *InssTek MX600* with a *SDM500* deposition nozzle inside a custom-built *MBraun* high-purity Ar inert gas enclosure (< 50-ppm residual H_2O and O_2). As energy source, an *IPG Photonics* (Oxford, USA) 1000-W continuous wave Yb:YAG Laser with 1070-nm wavelength and 0.5-mm spot size in the working plane was used. This DED subcategory is referred to as Laser Metal Deposition (LMD). Two Ar-atomized powders were used with nominal size ranges of 0.045–0.15 mm and nominal chemical compositions of TiAl48Cr2Nb2 and TiAl45Nb4C0.48. These alloys will henceforth be referred to as alloy A and alloy B, respectively.

The substrates were thermally insulated from the machine table trough 10-mm-thick graphite felt to decrease the heat flow from the substrate, lower the cooling rates, and increase the built temperature. The substrates measured roughly 15 mm × 15 mm × 10 mm and had a nominal composition of TiAl6V4 (wt%). For the miniature specimens, cuboids with 11-mm CAD edge length and 15 or 20 mm height, hatched in a cross snake pattern over the whole CAD slice without a contour path were produced. The hatching distance of the scan lines was set to 0.4 mm to achieve sufficient overlap of the meltpool tracks. The slicing height was set to 0.2 mm. The scan speed of the deposition nozzle was 20 mm/s and the laser power was 280 W. The parameters and substrate insulation are the result of prior experiments to produce dense, crack-free TiAl samples without additional heating in the LMD process. The energy input has to be high enough to suppress cracking but not too concentrated to minimize aluminum evaporation.

The powders were fed with a powder gas flow of 2 l/min per feeder and total mass flow rates of around 0.7 g/min through a coaxial nozzle into the melt pool to gain the desired compositions in the TiAl system. The specimens will be designated as follows: A and B stand for monolithic single alloy blocks of TiAl48Cr2Nb2 and TiAl45Nb4C. Specimens AB with no intentional material gradient (direct transition) were compared with samples A|||B with a 12 layer wide (~ 2.4 mm) gradient, which was produced with three different powder mass flow combinations between the two alloys A and B in vertical Z-direction. Additional cylinders with a CAD diameter of 10.5 mm and a height of 63 mm were produced using the same parameters for bulk testing.

Microstructure characterization

Samples for differential scanning calorimetry (DSC) in a *Netzsch STA 409 CD* were cut from an as-built LMD-produced A|||B specimen with a wider three step gradient stretched over 75 layers (~ 15 mm) to analyze the change of the phase transition temperatures with the changing compositions. Calphad calculations using the *Thermo-Calc* software with their TCTI database

version 2.2 were performed and compared to the experimental results.

Cross-sections were prepared by grinding on SiC paper, followed by mechanical and chemo-mechanical polishing. Electrochemical etching was employed for the grain size evaluation. Electron probe microanalysis (EPMA) mappings for the heat-treated state were recorded on a *JEOL JXA 8100* and compared. Further qualitative and quantitative scanning electron microscopy (SEM) analysis was performed using an *FEI Quanta 450* equipped with an *EDAX EDS* system, e.g., to determine the composition of DSC or mechanical testing specimens.

Heat treatment

The LMD samples were cut from the substrates and the surfaces ground on SiC paper to remove potential oxygen enrichment before the heat treatment was conducted in a vacuum furnace under 1.5×10^{-5} mbar. The heat treatment for the compositionally graded and bulk specimens consisted of a stress-free annealing at 650 °C for 2 h (in accordance to Arenas et. al. [29]) and a holding segment at 1320 °C for 10 min, which corresponds to a $\alpha + \gamma$ two-phase region for alloy A and a α single-phase region for alloy B. Compositionally uniform samples were also heat treated at further temperatures, shown in Table 1 in the results section, that correspond to the single-phase region for alloy A and the two-phase region for alloy B. The heating and cooling rates were 5 K/min. Cooling below 650 °C was uncontrolled furnace cooling.

Mechanical test specimen production

Mechanical performance of the deposited compositionally uniform (monolithic) and multi-material blocks was mainly evaluated by miniaturized tensile test (MTT) and miniaturized fracture toughness test through compact tension tests (MCT). The samples were extracted by wire eroding. The cutting plan for monolithic and multi-material block types is presented in Figure S 4 of supplementary material. In the case of monolithic blocks, the MTT specimens were extracted in two orientations XY perpendicular to the built direction and Z parallel to the built direction. The monolithic MCT specimens were extracted in the ZXE orientation, i.e., the crack growth direction is parallel to the build direction.

In the case of multi-material blocks MTT specimens were only tested in Z-direction to evaluate the influence of the material transition on the tensile properties. The MCT specimens were extracted in two different orientations: the ZXE orientation was the same as in the case of monolithic blocks with the additional constraint that specimens were extracted to allow the crack grow across the materials interface. Furthermore,

XZM-oriented specimens with a horizontally oriented crack plane perpendicular to the build direction placed at the estimated transition location between alloy A and B were produced. For each multi-material block the material interface position was established using light microscope observation. In order to reveal the different material structures at the interface, each block was firstly polished and etched using Kroll's Reagent. Based on these measurements the MCT specimen extract positions were suggested. Additional bulk cylindrical tensile specimens were machined out of LMD-produced cylinders in Z-orientation for the monolithic alloys and direct transition specimens A, B, and AB. The technical drawings of all specimen types can be found in the Supporting Information.

Miniature tensile testing

MTT specimens were tested according to ČSN EN ISO 6892-1 standard employing an electromechanical testing system *Tira Test* with a 10-kN load cell. Specimens were mounted by a manual gripping system. A virtual extensometer *Mercury RT* system with a single camera was used for the strain measurement, for which a contrast pattern of random speckles was sprayed on the specimen surface. An initial gage length of 4 mm was applied, based on the specimen initial cross-sectional dimensions and the gage length calculation for proportional tensile specimens with a proportionality factor $k = 5.65$. Specimens were tested under quasi-static loading conditions at a strain rate of 2.5×10^{-4} s^{-1} at room temperature.

Miniature compact tension testing

MCT specimens were tested for the fracture toughness characterization according to ASTM E 399 [30] and ASTM E 1820 [31]. However, due to the extreme brittleness of the material, applying a standard pre-cracking procedure was not viable, as the specimens suddenly failed during the procedure at a relatively low loading force. Therefore, MCT specimens were tested without pre-cracking. Furthermore, no side grooves were machined on the specimens. The testing procedure itself consisted of a quasi-static loading segment until the brittle fracture occurred.

In the current case, due to the small dimensions of the specimens, displacement of the specimen could not be measured at the load line position. Therefore, the displacement was monitored during the loading at the front face position using a COD extensometer. The crack mouth opening displacement (CMOD) values are recalculated to the corresponding load line displacement values according to

$$v_{\text{LL}} = \frac{\sqrt{\frac{a^2 + W^2}{2}}}{z + \sqrt{\frac{a^2 + W^2}{2}}} \cdot v_{\text{FF}}, \tag{1}$$

where a is the crack length, W represents the width of the specimen, z is the front face position of the COD extensometer, and v_{FF} is the corresponding CMOD measured at the front face [32].

Based on the force-load line records, the fracture toughness was evaluated. For all specimens, three different evaluation methods were used. The stress intensity factor (SIF) as K_{IC} parameter was evaluated using the 95% secant line method according to ASTM E 399 [30]. K_{IC} was also evaluated using the maximum force of the record, as in some cases the secant line and the record did not intersect. To account for specimens that showed a tendency for stable crack growth behavior, evaluation using the J-integral according to ASTM E 1820 [31] was added and fracture toughness was expressed as the K_{JC} parameter. This was done because using the more conservative 95% secant line method would exclude a considerable part of the curve from the evaluation process and SIF would be inadequate with respect to the material behavior.

Acknowledgments

Author contributions

FG contributed to investigation, formal analysis, and writing of the manuscript. DM contributed to investigation (mechanical miniature testing), formal analysis, and writing of the manuscript. JD, ZZ, and CK contributed to supervision, scientific discussion, and reviewing and editing of the manuscript. JD and CK contributed to funding acquisition.

Funding

Data availability

Electronic Supporting Information is available.

Declarations

Conflict of interest On behalf of all authors, the corresponding author states that there is no conflict of interest.

Open Access

Supplementary Information

The online version contains supplementary material available at https://doi.org/10.1557/s43578-022-00801-0.

References

1. H.A. Soliman, M. Elbestawi, Titanium aluminides processing by additive manufacturing—a review. Int. J. Adv. Manuf. Technol. **1760**, 67 (2022). https://doi.org/10.1007/s00170-022-08728-w

2. Y.-W. Kim, S.-L. Kim, Advances in gammalloy materials–processes–application technology: successes, dilemmas, and future. JOM **70**(4), 553–560 (2018). https://doi.org/10.1007/s11837-018-2747-x

3. H. Clemens, W. Smarsly, Light-weight intermetallic titanium aluminides—status of research and development. Adv. Mater. Res. **278**, 551–556 (2011). https://doi.org/10.4028/www.scientific.net/AMR.278.551

4. B.P. Bewlay, S. Nag, A. Suzuki et al., TiAl alloys in commercial aircraft engines. Mater. High Temp. **33**(4–5), 549–559 (2016). https://doi.org/10.1080/09603409.2016.1183068

5. Y.-W. Kim, D.M. Dimiduk, Progress in the understanding of gamma titanium aluminides. JOM **43**(8), 40–47 (1991)

6. P.J. Maziasz, C.T. Liu, Development of ultrafine lamellar structures in two-phase γ-TiAl alloys. Metall. Trans. A **29**(1), 105–117 (1998)

7. M. Schloffer, Gefüge und Eigenschaften der intermetallischen TNM-Legierung. Dissertation (2013)

8. D. Cormier, O. Harrysson, T. Mahale et al., Freeform fabrication of titanium aluminide via electron beam melting using prealloyed and blended powders. Res. Lett. Mater. Sci. **2007**, 1–4 (2007). https://doi.org/10.1155/2007/34737

9. L.E. Murr, S.M. Gaytan, A. Ceylan et al., Characterization of titanium aluminide alloy components fabricated by additive manufacturing using electron beam melting. Acta Mater.

58(5), 1887–1894 (2010). https://doi.org/10.1016/j.actamat.2009.11.032

10. M. Reith, M. Franke, M. Schloffer et al., Processing 4th generation titanium aluminides via electron beam based additive manufacturing—characterization of microstructure and mechanical properties. Materialia **14**, 100902 (2020). https://doi.org/10.1016/j.mtla.2020.100902

11. J. Gussone, Y.-C. Hagedorn, H. Gherekhloo et al., Microstructure of γ-titanium aluminide processed by selective laser melting at elevated temperatures. Intermetallics **66**, 133–140 (2015). https://doi.org/10.1016/j.intermet.2015.07.005

12. X.D. Zhang, C. Brice, D.W. Mahaffey et al., Characterization of laser-deposited TiAl alloys. Scr. Mater. **44**(10), 2419–2424 (2001). https://doi.org/10.1016/S1359-6462(01)00915-0

13. V.K. Balla, M. Das, A. Mohammad et al., Additive manufacturing of γ-TiAl: processing, microstructure, and properties. Adv. Eng. Mater. **18**(7), 1208–1215 (2016). https://doi.org/10.1002/adem.201500588

14. D. Melzer, J. Džugan, M. Koukolíková et al., Structural integrity and mechanical properties of the functionally graded material based on 316L/IN718 processed by DED technology. Int. Symp. Metall. Technol. Titan. Alloys **811**, 141038 (2021). https://doi.org/10.1016/j.msea.2021.141038

15. J. Dzugan, M. Sibr, P. Konopík et al., Mechanical properties determination of AM components. IOP Conf. Ser.: Mater. Sci. Eng. **179**, 12019 (2017). https://doi.org/10.1088/1757-899X/179/1/012019

16. K. Mertová, J. Džugan, M. Roudnická, M. Daniel, D. Vojtěch, M. Seifi, J.J. Lewandowski, Build size and orientation influence on mechanical properties of powder bed fusion deposited titanium parts. Metals **10**(10), 1340 (2020). https://doi.org/10.3390/met10101340

17. B. Strnadel, J. Brumek, The size effect in tensile test of steels, in *2013 proceedings of the ASME 2013 pressure vessels and piping conference (PVP2013)*. ed. by American Society ofMechanical Engineers (2013)

18. V.T. Witusiewicz, A.A. Bondar, U. Hecht et al., The Al–B–Nb–Ti system: IV. Experimental study and thermodynamic re-evaluation of the binary Al–Nb and ternary Al–Nb–Ti systems. J. Alloys Compd. **472**(1–2), 133–161 (2009). https://doi.org/10.1016/j.jallcom.2008.05.008

19. M. Thomas, T. Malot, P. Aubry, Laser metal deposition of the intermetallic TiAl alloy. Metall. Mater. Trans. A **48**(6), 3143–3158 (2017). https://doi.org/10.1007/s11661-017-4042-9

20. B. Lin, W. Chen, Y. Yang et al., Anisotropy of microstructure and tensile properties of Ti–48Al–2Cr–2Nb fabricated by electron beam melting. J. Alloys Compd. **830**, 154684 (2020). https://doi.org/10.1016/j.jallcom.2020.154684

21. V. Juechter, M.M. Franke, T. Merenda et al., Additive manufacturing of Ti-45Al-4Nb-C by selective electron beam melting for automotive applications. Addit. Manuf. **22**, 118–126 (2018). https://doi.org/10.1016/j.addma.2018.05.008

22. J. Lou, W.O. Soboyejo, An investigation of the effects of loading rate on resistance-curve behavior and toughening in cast lamellar gamma-based titanium aluminides. Metall. Mater. Trans. A **32**(2), 325–337 (2001). https://doi.org/10.1007/s11661-001-0264-x

23. T. Leitner, M. Schloffer, S. Mayer et al., Fracture and R-curve behavior of an intermetallic β-stabilized TiAl alloy with different nearly lamellar microstructures. Intermetallics **53**, 1–9 (2014). https://doi.org/10.1016/j.intermet.2014.04.005

24. M. Enoki, T. Kishi, Effect of rate on the fracture mechanism of TiAl. Int. Symp. Metall. Technol. Titan. Alloys **192–193**, 420–426 (1995). https://doi.org/10.1016/0921-5093(94)03244-0

25. A. Lintner, R. Pippan, M. Schloffer et al., Quasi-static and dynamic fracture toughness of a γ-TiAl alloy: measurement techniques, fractography and interpretation. Eng. Fract. Mech. **258**(4), 108081 (2021). https://doi.org/10.1016/j.engfracmech.2021.108081

26. S. Eck, J. Maierhofer, C. Tritremmel et al., Fatigue crack threshold analysis of TiAl SENT and CC specimens—influence of starter notch and precracking. Intermetallics **121**(5), 106770 (2020). https://doi.org/10.1016/j.intermet.2020.106770

27. O. Akourri, M. Louah, A. Kifani et al., The effect of notch radius on fracture toughness JIc. Eng. Fract. Mech. **65**(4), 491–505 (2000). https://doi.org/10.1016/S0013-7944(99)00109-5

28. ASTM International F42 Committee, *Terminology for additive manufacturing technologies (F2792)* (2012)

29. M.F. Arenas, V.L. Acoff, The effect of postweld heat treatment on gas tungsten arc welded gamma titanium aluminide. Scr. Mater. **46**(3), 241–246 (2002). https://doi.org/10.1016/S1359-6462(01)01232-5

30. ASTM International E08 Committee, *Test method for linear-elastic plane-strain fracture toughness of metallic materials (E399–20A)* (2020)

31. ASTM International E08 Committee, *Test Method for Measurement of Fracture Toughness (E1820–21)* (2021)

32. B.N. Rao, A.R. Acharya, Evaluation of Jc from the recorded front face displacement on ct specimens. Eng. Fract. Mech. **24**(4), 625–628 (1986). https://doi.org/10.1016/0013-7944(86)90235-3